Climatological study of the ion temperature in the ionosphere as recorded by Millstone Hill incoherent scatter radar and comparison with the IRI model

Alessio Pignalberi[1], Kateryna D. Aksonova[2,3], Shun-Rong Zhang[4], Vladimir Truhlik[5], Padma Gurram[6], Pavlou Charalambos[7]

[1] Istituto Nazionale di Geofisica e Vulcanologia, Via di Vigna Murata 605, 00143, Rome, Italy
[2] Institute of Radio Astronomy, National Academy of Sciences of Ukraine, 4, Mystetstv St., Kharkiv, 61002, Ukraine
[3] Institute of Ionosphere, National Academy of Sciences of Ukraine and Ministry of Education and Science of Ukraine, 16, Kyrpychov St., Kharkiv, 61001, Ukraine
[4] Haystack Observatory, Massachusetts Institute of Technology, 99 Millstone Rd, Westford, MA 01886, USA
[5] Institute of Atmospheric Physics of the Czech Academy of Sciences, Boční II 1401, 14100, Prague, Czech Republic
[6] Indian institute of geomagnetism, Kalamboli Highway, New Panvel Navi Mumbai, 410218, India
[7] Department of Electrical Engineering, Frederick University, Y. Frederickou Str. Pallouriotisa, 1036, Nicosia, Cyprus

Abstract

Ion temperature data recorded by Millstone Hill incoherent scatter radar (42.61° N, 288.51° E) over four full solar cycles (from 1970 to 2018) are analyzed to depict its climatological behavior in the range of altitudes between 100 and 550 km. The ion temperature dependencies on altitude, local time, month of the year, and solar activity level are studied through a climatological analysis based on binning and boxplot representation of statistical values. Binned observations of ion temperature are compared with International Reference Ionosphere (IRI) modeled values (IRI-2016 version). This comparison reveals several shortcomings in the IRI modeling of the ion temperature at ionosphere altitudes, in particular for the altitudinal, diurnal, seasonal, and solar activity description. The main finding of this study is that the overall IRI overestimation of the ion temperature can be probably ascribed to the long-term ionosphere cooling. Moreover, the study suggests that the IRI ion temperature model needs to implement the seasonal and solar activity dependence, and introduce a more refined diurnal description to allow multiple diurnal maxima seen in observations. The IRI ion temperature anchor point at 430 km is investigated in more detail to show how also a better description of the altitude dependence is desirable for modeling purposes. Some hints and clues are finally given to improve the IRI ion temperature model.

Keywords: Ion temperature, Millstone Hill incoherent scatter radar, International Reference Ionosphere model, Climatological analysis.

Corresponding author: Alessio Pignalberi (alessio.pignalberi@ingv.it)

Co-authors e-mails: Kateryna D. Aksonova (katya.aksen93@gmail.com), Shun-Rong Zhang (shunrong@mit.edu), Vladimir Truhlik (vtr@ufa.cas.cz), Padma Gurram (padmagurram123@gmail.com), Pavlou Charalambos (charalambos.pavlou.13@gmail.com)

1. Introduction

During the 50s and 60s a large amount of ionospheric plasma temperature observations from satellites, rockets and ground-based facilities became available (Willmore, 1970). It soon appeared that the temperature of the charged particles generally exceeds the neutrals one by a factor that depends on the altitude and that is highly variable with time and location. Then, the ionosphere, for a large part, is not in thermal equilibrium. This fact has a quantity of physical implications for the ionosphere that makes very interesting and important the study of the electron and ion temperature. Notably, the temperature of charged particles deeply influences the distribution of the electron density in the ionosphere; in the topside ionosphere (the region above the absolute maximum in the electron density) because of its diffusive equilibrium state (Rishbeth and Garriott, 1969;

Ratcliffe, 1972), and in the bottomside ionosphere (the region below the absolute maximum in the electron density) by modifying the rate of recombination at those altitudes (Rishbeth and Garriott, 1969; Ratcliffe, 1972).

Theoretical studies and observations (Banks, 1967; Roble, 1970; Willmore, 1970; Schunk and Nagy, 1978; and references therein) revealed that the major sources of energy heating the ionosphere are the solar EUV and X-ray radiations, except for high latitudes and under disturbed conditions. The EUV and X-ray solar radiation photons ionize the neutral particles of the ionosphere by producing photo-electrons whose excess of kinetic energy dissipates through collisions with neutrals and charged particles. In the ionization process, the excess of energy is shared between electrons and ions but, because of their significantly smaller mass, electrons gather most of it. In an early stage, collisions between electrons rapidly distribute the excess of energy giving rise to an increase of the electron temperature (T_e) above the neutral one (T_n), because of the transfer of energy via elastic collisions is more efficient between particles of similar mass. Owing to the established temperature difference, the electrons begin to lose their excess of energy through collisions with surrounding particles and by downward conduction. Ion-electron Coulomb collisions are more efficient than neutral-electron collisions, then the ion temperature (T_i) first increases. The ions, in turn, lose their excess of energy through collisions with neutrals and ions. Because of this, the following inequalities apply in the ionosphere $T_n(h) \leq T_i(h) \leq T_e(h)$ in a wide range of altitudes. As a result of these interactions, the entire photo-electrons energy dissipates in the neutrals and is finally removed by downward conduction and radiation.

Due to the very low heat capacity of electrons, T_e is found to be highly variable in time being very responsive to changes in the solar radiation energy input (Banks, 1967). Furthermore, due to the close coupling with the geomagnetic field lines and plasmasphere, very distinct spatial patterns characterize T_e (Schunk and Nagy, 1978). In contrast, ions exhibit a lower thermal variability due to their higher heat capacity. The T_i vertical profile in the ionosphere is determined by the balance between the heat gained through Coulomb collisions with electrons and lost through collisions with neutrals. Because of the observed distribution with height of neutrals (decreasing with altitude) and electrons (increasing with altitude in the bottomside and decreasing in the topside), the balance between heat gained and lost depends on altitude. T_i tends to converge to T_n at lower altitudes (below about 300 km) due to the very high density of neutrals (and then high collision frequency), and to T_e at higher altitudes (above about 1000 km). In the following, when considering the ion temperature, we do not differentiate among different ion species despite some small differences between the temperature of different ions can be found in the topside (Banks, 1967).

The main experimental techniques employed over the years to measure plasma temperatures are in-situ measurements taken by Langmuir Probes (LP) and Retarding Potential Analyzers (RPA) (Willmore, 1970; Bilitza, 1991) aboard satellites or rockets, and remote sensing measurements by Incoherent Scatter Radars (ISR) (Evans, 1969; Bilitza, 1991). LP and RPA on-board Low Earth Orbit (LEO) satellites give the opportunity to provide a global spatial description of measured plasma temperatures for different local times, depending on the orbit configuration. In contrast, ISR can better describe the time variability of plasma temperatures for a fixed location, thus highlighting diurnal, seasonal, and even solar activity variability when long time series become available. Both of them, over the years, provided a significant amount of plasma temperatures observations that were used as datasets for the development of empirical models. Bilitza (1991) compiled an exhaustive collection of LP, RPA, and ISR datasets available for ionospheric studies.

In this work, ion temperature observations collected by Millstone Hill ISR (42.61° N, 288.51° E) over a time period covering more than four solar cycles (from 1970 to 2018) were studied. We focused on the main climatological features of the ion temperature over a range of altitudes spanning from 100 to 550 km, by highlighting its altitudinal, diurnal, and seasonal behavior for different solar activity levels. As a climatological study, we restricted ourselves to magnetically quiet periods. The climatological trends that emerged from the analysis of Millstone Hill ISR T_i observations were compared to corresponding values modeled by the International Reference Ionosphere (IRI, Bilitza et al., 2017) model. IRI is the most popular empirical climatological model of the ionosphere in the ionospheric community, and it is recognized as the official ISO standard for the ionosphere (Bilitza, 2018). IRI provides monthly averages of the electron density, electron temperature, ion temperature, and ion composition in the ionospheric altitude range, on a global basis, for different levels of solar and magnetic activity.

Many authors in the past described the main features of the ion temperature as recorded by ISRs, for different locations and time periods (Evans, 1967, 1970; Bilitza, 1984, 1987; Holt et al., 2002; Holt and Zhang, 2008; Oliver et al., 1991: Otsuka et al., 1998; Roble, 1975; Roble et al., 1978; Zhang and Holt, 2004, 2007, 2008, 2013; Zhang et al., 2004, 2005a, 2005b, 2007, 2011, 2016). Zhang et al. (2004, 2007) and Zhang and Holt (2004) made comparisons between ion temperature data measured by several ISRs and modeled by IRI. In particular, Zhang and Holt (2004) described the climatological features of plasma temperatures by analyzing observations collected by Millstone Hill ISR from 1976 to 2001, and compared them with IRI for different seasons, local times, and altitudes. They found that IRI shows a good agreement with ion temperature observations at 300 km and above; while, at lower altitudes, IRI overestimates the observed ion temperature, particularly during nighttime.

Our work intends to further extend the climatological study of the ion temperature made by Zhang and Holt (2004) through the use of a more extensive dataset; and, by comparison with IRI, to give valuable clues to improve IRI modeling of this important ionospheric parameter.

In Section 2, the ion temperature dataset collected by Millstone Hill ISR is presented along with the binning procedure applied to highlight altitudinal, diurnal, seasonal, and solar activity dependencies. In the same section, the IRI ion temperature model is described in depth. Finally, an example of the statistical methodology applied to obtain the results of Section 3 is discussed. Section 3 contains the results of the climatological analysis of Millstone Hill ion temperature obsearvations and the comparison with IRI modeled values for the same geophysical conditions. Firstly, we studied the altitude variation of the ion temperature for different seasons, local time (LT), and solar activity levels. Secondly, we focused on the ion temperature at about 430 km of height, that is an anchor point for the IRI modeled ion temperature vertical profile. In Section 4, the main results of this study are summarized and discussed, by also providing valuable clues on how to improve the IRI model.

2. Data and Method

2.1 Millstone Hill ISR facility

Millstone Hill ISR includes two antennas located at Haystack Observatory, Westford, MA (42.61°N, 288.51°E, Apex magnetic latitude = 53.4°N). It operates with a zenith-directed 68 m fixed parabolic and a fully-steerable 46 m diameter antenna in the UHF-range band. Transmitters operate at a frequency of 440 MHz with the peak power 2.5 MW (Holt et al., 2002, Zhang et al., 2004). The ISR exploits Thomson backscatter from ionospheric electrons. Transmitted radio waves cause electrons vibrations in the ionosphere, which subsequently emit a small amount of their own energy. This energy is the return signal, which is observed as a joint emission from a group of electrons ("incoherent”). ISR facilities are capable of measuring important ionospheric parameters, including ion and electron temperatures, plasma velocity, and electron density (Evans, 1969). Such technique provides observations of full atmospheric altitude profiles of the plasma state at altitudes extending from about 100 km to a thousand kilometers. ISR observations at Millstone Hill utilize multiple waveforms of radio signals. Normally, the long pulses with considerable returning signal-to-noise ratio and reasonable time-altitude resolution are most appropriate for the F region study, and the coded pulse scheme is appropriate for the E/F1 region study. For the purpose of this study, we selected observations using the long-pulse at 480 μs or shorter above 250 km, and Alternating Code below 250 km. To determine the ion temperature from ISR measurements, it is common to assume a model of the molecular ion composition relative to the atomic oxygen ion. At Millstone Hill a standard composition model has been used with a fixed height, the Lower Transition Height (LTH), of equal O^+ density and molecular ion density at 180 km. The true LTH will be local time, season, and solar cycle dependent, thus T_i from the standard LTH model is subject to a small bias near the F1 region. This small bias, as evaluated in Zhang et al. (2018), is 2% for a 10% uncertainty in the ratio of the molecular ion density over the total ion density, and 0.2% if the ratio is subject to a 1% long-term trend. All data used in this paper are archived in the Millstone Hill Madrigal online database system (http://madrigal.haystack.mit.edu/madrigal/).

2.2 Ion temperature dataset

The dataset used in this study consists of ion temperature observations collected by Millstone Hill ISR (Evans, 1969) between years 1970 and 2018. The temporal distribution of data along this very extended time period is given in Figure 1 as cumulated hours of operation of the Millstone Hill ISR for each year. Data availability sharply increases in 1976, due to the installation of a new antenna, and steadily grows over the years. The dataset covers more than four solar cycles, thus representing the longest record of the ion temperature so far studied.

We restricted our analysis to magnetically quiet periods in order to focus on the climatological behavior of the ion temperature. In this regard, the collected observations were filtered by considering the three-hourly values of the geomagnetic index *ap* (Rostoker, 1972) as a proxy of the geomagnetic activity level. Specifically, Millstone Hill ISR runs performed when *ap* > 15 nT were discarded. In this way, we excluded about 25% of the original dataset. Values reported in Figure 1 represents data already filtered for the geomagnetic activity level.

Furthermore, we studied different levels of the solar activity. Data were binned in three solar activity level bins by considering the 81-days running mean of the F10.7 index ($F10.7_{81}$). F10.7 is the solar radio flux at 10.7 cm (2800 MHz) (Tapping, 2013) and represents one of the most used solar activity proxy for ionospheric modeling. In particular, we calculated its 81-days running mean in order to smooth the short-time variability which is beyond the scope of this climatological study (Figure 1). The solar activity binning is the following:

- Low solar activity level: $F10.7_{81} < 100$ s.f.u. (solar flux units, 1 s.f.u. $= 10^{-22}$ W m^{-2}), $\overline{F10.7_{81}} = 78.9$ s.f.u., 53.54% of the entire dataset;
- Moderate solar activity level: $100 \leq F10.7_{81} < 150$ s.f.u., $\overline{F10.7_{81}} = 120.2$ s.f.u., 28.48% of the entire dataset;
- High solar activity level: $F10.7_{81} \geq 150$ s.f.u., $\overline{F10.7_{81}} = 185.6$ s.f.u., 17.98% of the entire dataset.

Figure 1 shows both the $F10.7_{81}$ time series and the three solar activity bins with their thresholds.

To study the ion temperature dependence on height, we arranged data in twelve altitude bins depending on the data sampling and availability: 100-120 km, 120-140 km, 140-160 km, 160-180 km, 180-200 km, 200-250 km, 250-300 km, 300-350 km, 350-400 km, 400-450 km, 450-500 km, 500-550 km.

Furthermore, to identify the ion temperature diurnal and seasonal dependencies, we binned data as a function of local time and month of the year. Specifically, we grouped data in 12 bins as a function of the month of the year, and in 24 bins as a function of the local time (LT) hour (bins of width one hour centered around each LT hour).

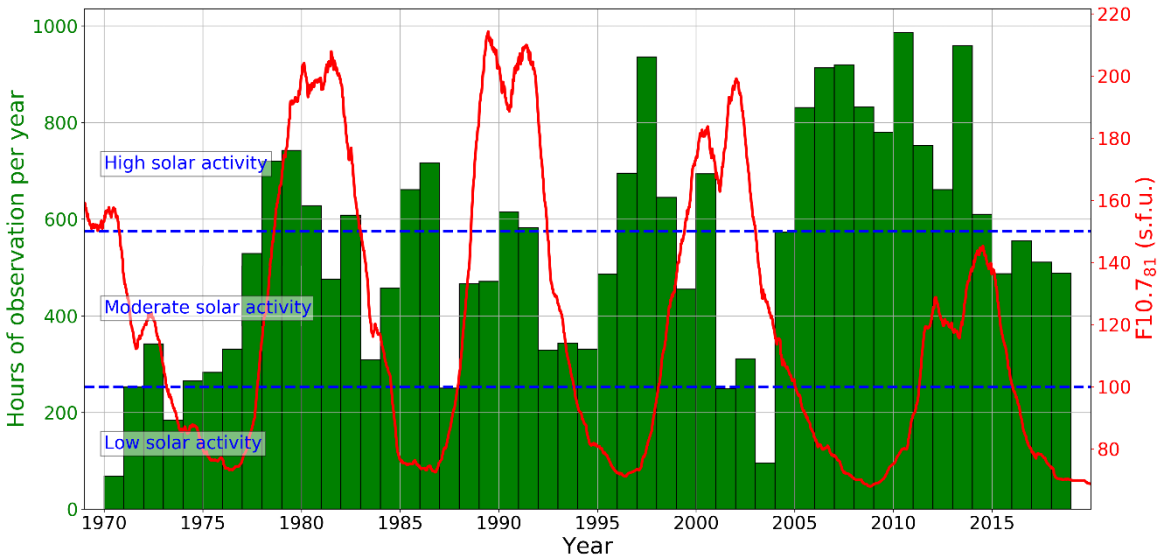

Figure 1: The histogram in green represents the Millstone Hill ISR hours of operation per year, from 1970 to 2018. The red line depicts the trend of the $F10.7_{81}$ solar activity proxy over the same time period. Horizontal blue dashed lines separate the three different solar activity levels identified in this study.

2.3 IRI modeling of the ion temperature

The ion temperature model embedded in IRI is based on the work of Bilitza (1981). Bilitza (1981) described the height dependence (altitude gradient above 430 km) of the ion temperature through ISRs observations (Jicamarca, Arecibo, Millstone Hill) (3K/km for day-time and 0K/km for nighttime), and its latitudinal and local time dependence at an altitude of 430 km through AEROS satellites data (AEROS-A, AEROS-B). Specifically, as reported in Table 1, Bilitza (1981) exploited data collected in 1960s and 1970s; years when the solar activity spanned from low to moderate. Moreover, except for data coming from Arecibo ISR, Bilitza (1981) used only day-time and nighttime ion temperature observations (in the case of AEROS satellites due to their orbit configuration). None seasonal or solar activity sorting of observations was made by Bilitza (1981) because the available dataset showed no clear dependency on them.

Type of data	**Geographic Latitude**	**Geographic Longitude**	**Data availability**	**R_{12}**	**$F10.7_{81}$ [s.f.u.]**	**Median values calculated for**
Arecibo ISR	18°N	293°E	7/1966-6/1970 12/1971-12/1972	50-100 58-73	108-176 99-135	Entire day
Jicamarca ISR	12°S	283°E	11/1966-4/1969	75-110	118-176	Day: 11-13 LT Night: 23-1 LT
Millstone Hill ISR	43°N	289°E	2/1972-10/1975	25-71	71-135	Day: 11-13 LT Night: 23-1 LT
AEROS-A satellite	Global	Global	12/1972-8/1973	40-50	87-107	Day: 14-16 LT Night: 2-4 LT
AEROS-B satellite	Global	Global	6/1974-9/1975	10-35	71-93	Day: 15-17 LT Night: 3-5 LT

Table 1: Data type, location, time availability, solar activity conditions, and binning used by Bilitza (1981) to model the ion temperature in IRI (adapted from Bilitza (1981)).

In the development of the IRI ion temperature model, also theoretical assumptions about its height distribution are considered, in particular:

$$T_{\mathrm{n}}(h) \le T_{\mathrm{i}}(h) \le T_{\mathrm{e}}(h) \qquad \forall h\ ; \tag{1}$$

T_{i} approaching T_{n} at lower altitudes, and T_{e} at higher.

Bilitza (1981) applied the Booker's mathematical approach (see Appendix) to get a smooth representation of the ion temperature vertical profile.

Specifically, Bilitza (1981) divided the ion temperature vertical profile $T_{\mathrm{i}}(h)$ into four different subsections (Figure 2):

$$T_{\mathrm{i}}(h) = \begin{cases} T_{\mathrm{n}}(h) & \text{for} \quad h \le HS \\ T_{\mathrm{i},k}(430,\varphi) + \dfrac{T_{\mathrm{i},k}(430,\varphi) - T_{\mathrm{n}}(HS)}{430 - HS}\left(h - 430\right) & \text{for} \quad HS \le h \le 430 \\ T_{\mathrm{i},k}(430,\varphi) + M_k\left(h - 430\right) & \text{for} \quad 430 \le h \le HTT \\ T_{\mathrm{e}}(h) & \text{for} \quad h \ge HTT \end{cases} . \tag{2}$$

T_i matches the neutral temperature T_n below *HS*, and the electron temperature T_e above *HTT* (Bilitza, 1990; Bilitza et al., 1993). *HS* is the altitude where T_i match T_n, located at around 200 km of altitude; it is the altitude where the tangent to the neutral profile passes through the ion temperature value at 430 km (Bilitza, 1981). However, IRI-2016 FORTRAN code implements *HS* = 200 km. *HTT* is the altitude where the T_i profile meets the T_e profile; it is highly variable, critically depending on the T_e profile modeling (Truhlik et al., 2009, 2012, 2015). Between *HS* and 430 km of altitude, and between 430 km and *HTT*, T_i varies in a linear way with different slopes. In fact, through the analysis of several ISRs observations, Bilitza (1981) found a distinct change in dT_i/dh at 430 km of altitude. Then, he modeled the ion temperature at 430 km of altitude $T_{i,k}(430, \varphi)$ through ISRs and AEROS satellites data. Specifically, Bilitza (1981) described the dependence on the geomagnetic latitude φ, and the different behavior between day-time (subscript k=1 in (2)) and nighttime hours (k=2 in (2)), of the ion temperature at 430 km of altitude with the following:

$$T_{i,k}(430,\varphi) = \begin{cases} T_{i,1}(430,\varphi) = 1240 - 1400\dfrac{\exp(-0.09\varphi)}{\left[1+\exp(-0.09\varphi)\right]^2} & \text{day-time} \\ T_{i,2}(430,\varphi) = 1200 - 300\dfrac{\cos(\chi)}{|\cos(\chi)|}\sqrt{|\cos(\chi)|} & \text{nighttime} \end{cases}, \tag{3}$$

with

$$\begin{cases} M_k = \begin{cases} M_1 = 3 & \text{day-time} \\ M_2 = 0 & \text{nighttime} \end{cases} \\ \chi(\varphi) = 0.47|\varphi| + 0.024\varphi^2 \end{cases}. \tag{4}$$

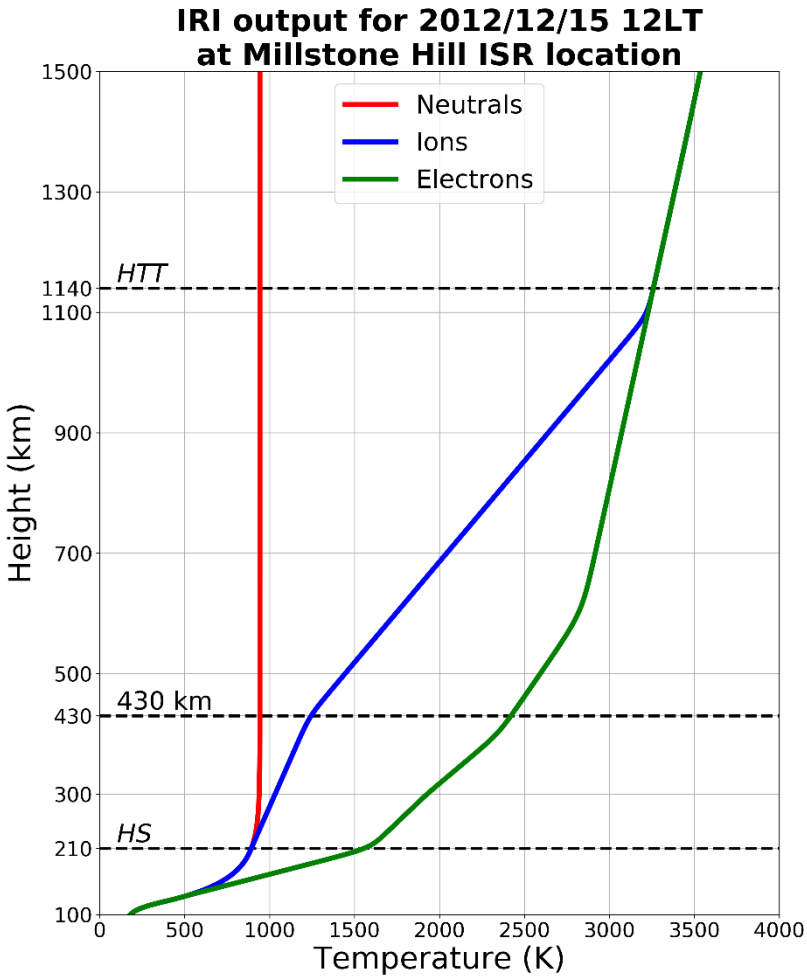

Figure 2: IRI modeled vertical profiles of the neutral (red line), ion (blue line), and electron (in green) temperature at Millstone Hill ISR location for 2012/12/15 at 12 LT. With horizontal dashed black lines are highlighted *HS*, 430 km, and *HTT* altitudes.

Finally, the Booker formalism (see Appendix) allows to produce smooth transitions of the ion temperature at 430 km and *HTT* (m=2 in (A3)), and to obtain a smooth and continuous description of the entire vertical ion temperature profile. Then, considering that $y \equiv dT_i/dh$ in (A2) and $Y \equiv T_i$ in (A3), and the parameters for the subsections identified in Table 2, the ion temperature is modeled through (A3).

j	$h_{s,j}$ [km]	$d_{s,j}$ [km]	y_j ($\equiv dT_i/dh$) [K/km]	Y_j ($\equiv T_i$) [K]
0	HS ($\equiv h_0$)		$\frac{T_{i,k}(430,\varphi)-T_n(HS)}{430-HS}$	$T_n(HS)$
1	430	10	M_k	$T_{i,k}(430,\varphi)$
2	HTT	10	$\frac{dT_e(HTT)}{dh}$	$T_e(HTT)$

Table 2: Parameters used by Bilitza (1981) in the Booker's approach to obtain the ion temperature vertical profile, as derived from (2)-(3).

As a consequence, two equations are obtained: the one with k=1 for the day-time behavior ($T_{\mathrm{i,day}}$) and the one with k=2 for the nighttime ($T_{\mathrm{i,night}}$). IRI considers only the variation due to the transition between day-time and nighttime values of the ion temperature at sunrise and sunset, modeled through Epstep functions (A1). Then, the diurnal variation of $T_{\mathrm{i,}}$ is (Bilitza, 1981):

$$T_{\mathrm{i}}(h,t) = T_{\mathrm{i,night}}(h) + \frac{T_{\mathrm{i,day}}(h) - T_{\mathrm{i,night}}(h)}{1+\exp\left(-\frac{t-t_{\mathrm{sr}}}{D}\right)} + \frac{T_{\mathrm{i,night}}(h) - T_{\mathrm{i,day}}(h)}{1+\exp\left(-\frac{t-t_{\mathrm{ss}}}{D}\right)}, \tag{5}$$

where t_{sr} and t_{ss} are the time of sunrise and sunset, respectively; while, D=1 hour is the transition time.

As stated by above equations, IRI does not explicitly describes the seasonal and solar activity variability in the ion temperature. However, because $T_{\mathrm{i}} = T_{\mathrm{n}}$ below HS and $T_{\mathrm{i}} = T_{\mathrm{e}}$ above HTT, and both T_{n} from the NRLMSISE-00 model (Picone et al., 2002) and T_{e} from Truhlik et al. (2012) (Bilitza et al., 1993, 2007; Truhlik et al., 2009, 2012, 2015) undergo seasonal and solar activity variations, corresponding dependence on them is expected also in T_{i}. However, several authors in the past highlighted the need of including an improved description of the solar activity dependence in the IRI ion temperature modeling (Buonsanto, 1989; Bilitza and Hoegy, 1990)

Furthermore, in the IRI code some constrains are placed in order to assure theoretical expectations (Bilitza, 1990): the ion, electron, and neutral temperatures are forced to be equal at $h = HTA$ =120 km, and corrections are applied in the case $T_{\mathrm{i}}(h) \geq T_{\mathrm{e}}(h)$.

2.4 Method of comparison between measured and modeled ion temperatures

Section 2.2 described how ion temperature observations were binned as a function of the solar activity level (3 bins), altitude (12 bins), LT hour (24 bins), and month of the year (12 bins). By means of this binning procedure, the entire ion temperature dataset (10216789 data points) was splitted in 10368 sub-datasets (3x12x24x12). For each sub-dataset, we calculated the following statistical quantities: median (50th percentile), first quartile (25th percentile), third quartile (75th percentile), 5th percentile, and 95th percentile. These statistical quantities are graphically represented as boxplots to easily infer the median ion temperature behavior for different conditions.

Figure 3 shows an example of boxplot representing ion temperature observations recorded by Millstone Hill ISR for low solar activity, June month, 12 LT (data between 11:30 and 12:30 LT), for the 12 altitude ranges. For each box, the solid horizontal green line is the median (a green point, placed at the center of the bin, indicates the median value), the upper and lower edges of the box (blue solid lines) depict the third and first quartile, respectively, while lines extending from the box (whiskers) indicate the variability outside the upper and lower quartiles until 95th and 5th percentiles, respectively. For each box, the number of data inside the box is indicated in the below histogram, in shadowed orange. The green dashed line joins the median measured ion temperature values. Red points, connected by a red dashed line, represent the ion temperature values modeled by IRI, for the same conditions. Specifically, this example represents an IRI run for the year 2010, 15th of June, 12 LT, for altitudes from 110 to 525 km with 5 km steps, for the Millstone Hill location.

In this analysis, IRI was run for the 15th day of the considered month, for the hh local time (where $hh \in [0;23]$), and for the year 2010 for low solar activity, 2012 for moderate solar activity, and 1990 for high solar activity. In fact, because IRI does not explicitly model the dependence of the ion temperature on solar activity, to represent this, we selected three years whose solar activity level is as close as possible to $\overline{\mathrm{F10.7}}_{81}$ values calculated for the three selected solar activity levels (Section 2.2).

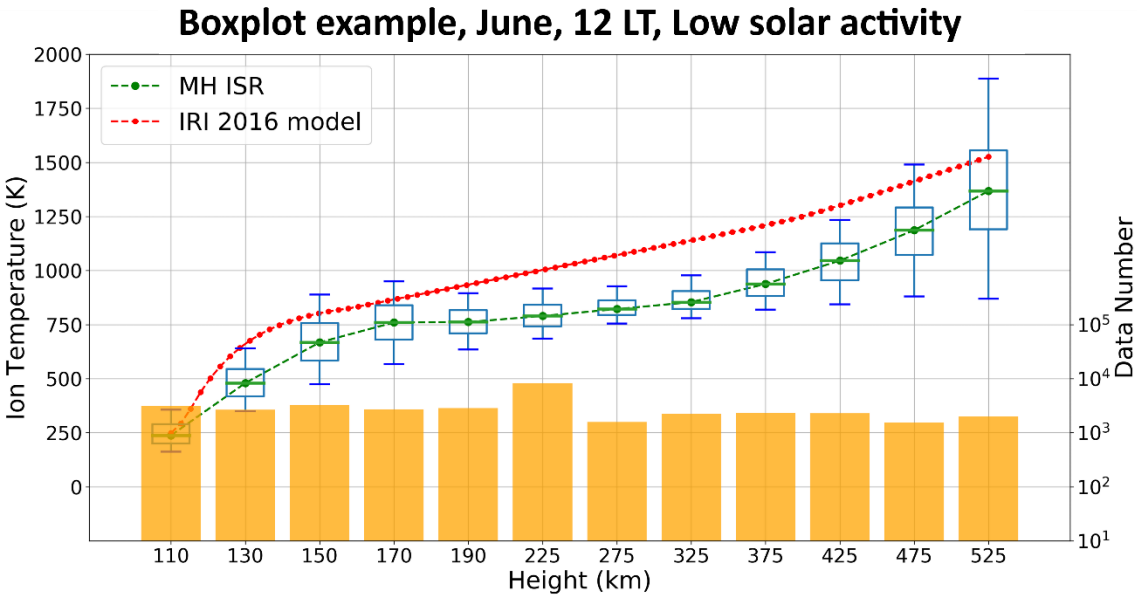

Figure 3: Boxplot statistical analysis example by using ion temperature observations collected by Millstone Hill ISR from 1970 to 2018, for low solar activity level, for the month of June, around 12 LT.

Figure 3 shows that the boxplot representation is particularly suited for the representation of binned data in order to visually highlight the median behavior (and the corresponding dispersion around median values) of a large amount of data in a simple and straightforward way. The statistical parameter describing the dispersion of data is the interquartile range (IQR), i.e., the difference between the upper and the lower quartiles. In the boxplot analysis no assumption is made on the statistical distribution of data inside the bin; nevertheless, the symmetry of the box, with respect to the median, indicates that the distribution is symmetric around the median value.

3. Results and discussion

3.1 Overall description of the ion temperature variability over Millstone Hill

In this section, we give an overall description of the ion temperature variability as a function of altitude, local time, month of the year, and solar activity level, for the Millstone Hill location. Specifically, we studied the seasonal variability by focusing on March, June, September, and December months, as representative of the equinoxes and solstices conditions. The diurnal variability is shown for the LT hours 0, 6, 12, and 18, as representative of the nighttime, dawn, day-time, and dusk conditions. The solar activity and altitude variabilities are studied following the binning procedure described in Section 2.2. Data are presented as described in Section 2.4.

Figures 4 to 7 represent boxplots of Millstone Hill ISR observations vs IRI-2016 modeled values for the months of March, June, September, and December, respectively. Top panels show the results for low solar activity, middle panels for moderate solar activity, and bottom panels for high solar activity. In this analysis, we do not consider ion temperature observations below 200 km at night (0 LT) due to their low reliability; then, corresponding boxes are not shown. It should be noted that the less availability of observations for high solar activity levels can lead to the impossibility to calculate statistical values in some cases (bottom panels of Figure 4 and 5).

Looking at Figures 4 to 7, it clearly emerges that the agreement between IRI and ISR observations is higher during day-time hours compared to nighttime. In particular, the best agreement is for 12 LT hour; a similar behavior is exhibited by solar terminator hours (6 and 18 LT), while a visible performance degradation is notable for 0 LT. Moreover, IRI exhibits better performances for the summer season (June), a lower agreement for equinoxes months (March and September), while a remarkable worsening in the winter season (December).

These considerations will be statistically evaluated in the next section by considering statistical quantities between measured and modeled values.

It is very remarkable the IRI overall overestimation of measured ion temperatures for most of the conditions represented in Figures 4 to 7. The IRI overestimation is particularly emphasized for lower altitudes, winter season, and low solar activity level. A first explanation of the IRI overestimation might be linked to the dataset and the empirical relations employed by Bilitza (1981) to model the ion temperature, as described in Section 2.3; however, a physical explanation can be found in the long-term decreasing trend of the ion temperature in the ionosphere. Indeed, as recently demonstrated by several authors (Holt and Zhang, 2008; Zhang and Holt, 2013; Zhang et al., 2011, 2016, Laštoviča, 2017), the ionosphere is undergoing a general cooling since first plasma temperatures were measured back in 1960s and 1970s. Independent ionospheric/thermospheric observations show that the upper atmosphere is cooling since the 1970s, when the global warming in the atmosphere become gradually apparent. At ionospheric altitudes, this may be up to 50-100 K in a period of 50 years (Zhang et al., 2016), so this long-term cooling may provide a partial contribution to the IRI and Millstone Hill data difference. The IRI ion temperature model in the F-region is primarily based on data measured prior to 1980s (see Table 1), so IRI represents the ion temperature median behavior before 1980s. However, observations presented in this work span a very long time with the majority of data after 1980s, then it is biased toward most recent years. Hence, due to the observed long-term ionosphere cooling, an overestimation for IRI is expected and fully understandable.

Both modeled and measured T_i values exhibit a dependence on solar activity. It is worth noting that the IRI model does not explicitly account for the solar activity dependence in the T_i modeling; however, due to its close coupling with the neutral temperature below and the electron temperature above (see Section 2.3), it also exhibits an implicit dependence on solar activity. Nonetheless, as also pointed out by Buonsanto (1989) and by Bilitza and Hoegy (1990), the IRI T_i model needs an explicit dependence on the solar activity. The dataset shown in Table 1 is highly biased toward low and moderate solar activity, then a more extensive dataset covering a wider range of solar activities is needed. From this point of view, the dataset here presented might be very helpful covering a wide range of solar activity levels for different solar cycles.

It should be noted that IRI T_i does not explicitly account for the seasonal dependence, whilst observations exhibit it. The fact that the IRI performances are better for June is a clue that the original dataset on which IRI T_i is based might be biased toward summer months. Hence, the very poor performances during winter months. Also in this case, an improvement of the IRI T_i model based on the introduction of a seasonal dependence is desirable. Noteworthy is the higher dispersion exhibited by T_i observations for December, above all at low solar activity and high altitudes. This is due to an intrinsic higher variability of the T_i in the winter season that makes undoubtedly more difficult to model it in this season.

As stated by Eq. (5), IRI smoothly goes through a nighttime to a day-time behavior at solar terminator hours; however, it does not allow for any variation during nighttime and day-time hours. The better performances exhibited for 12 LT hours compared to solar terminator hours (6 and 18 LT) are an evident clue that a more refined diurnal description of T_i is needed because measured T_i observations exhibit a more complex diurnal trend. Of course, the IRI diurnal behavior is strictly constrained by the originally used dataset which is for the most based on day-time and nighttime hours. The better coverage of different local time hours of the dataset used in this study might be exploited with profit to implement a better diurnal description of T_i in IRI.

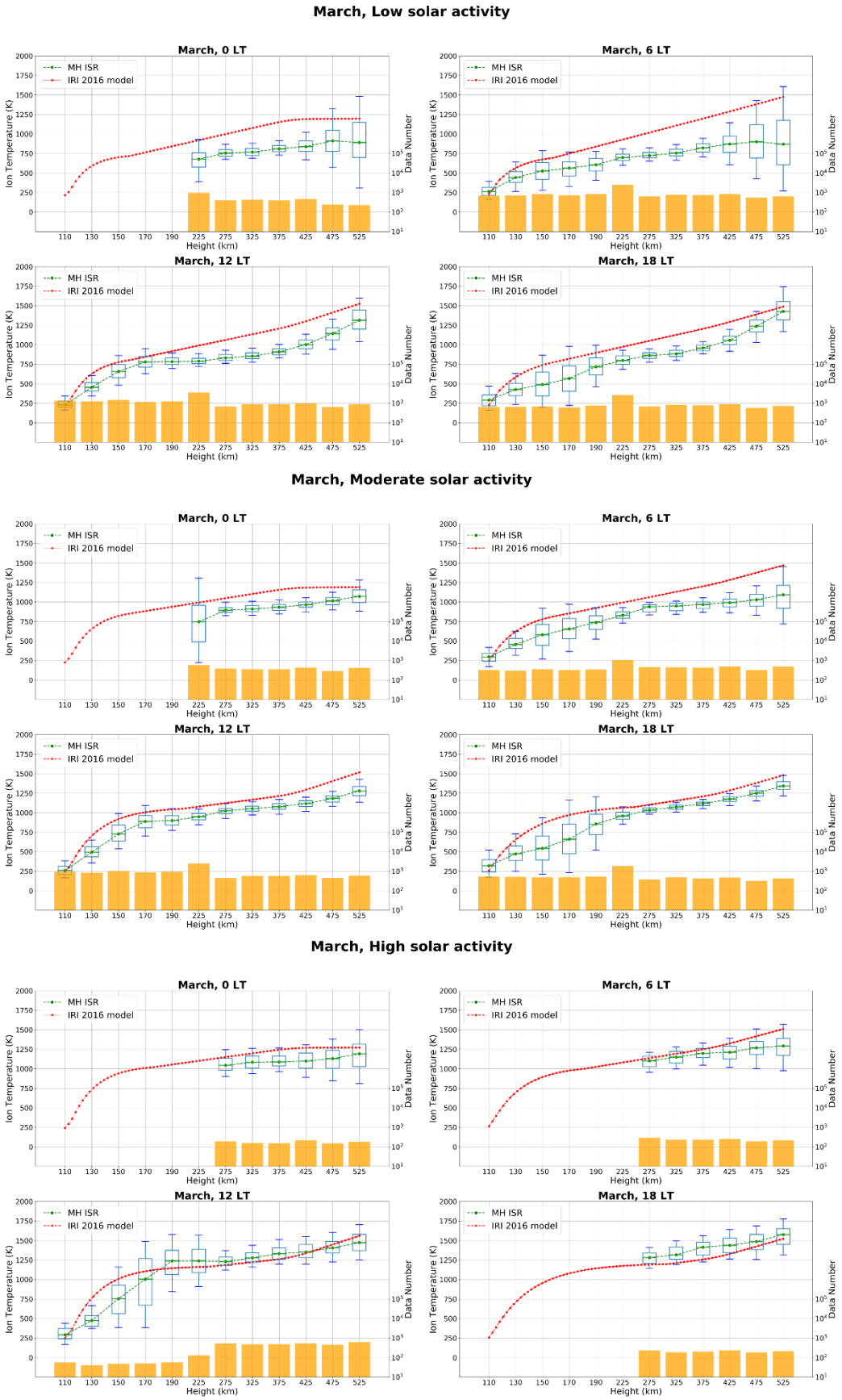

Figure 4: Boxplot statistical analysis for March, for different LT hours (0,6,12,18), for low (top panels), moderate (middle panels), and high (bottom panels) solar activity levels.

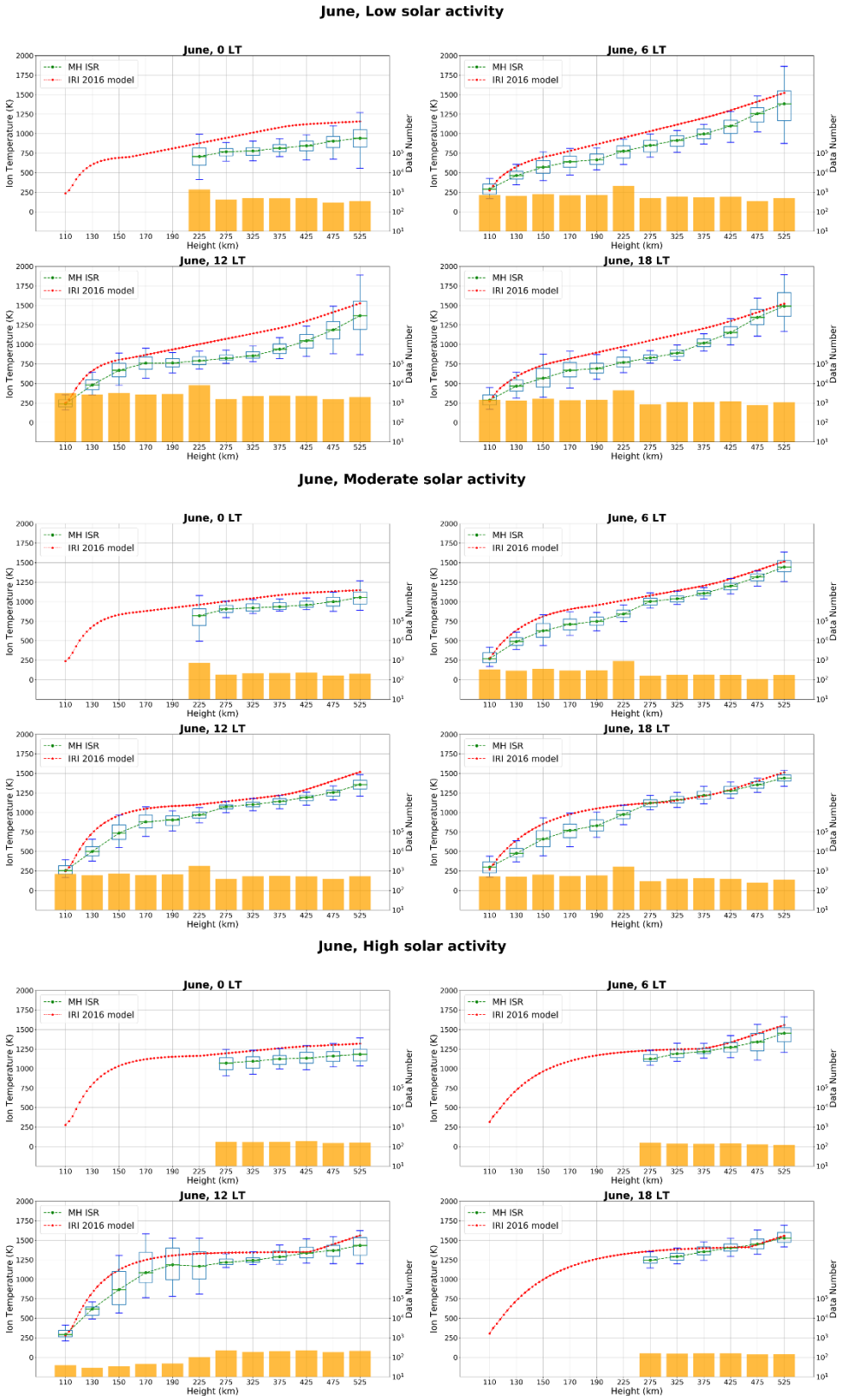

Figure 5: Same as Figure 4, but for June.

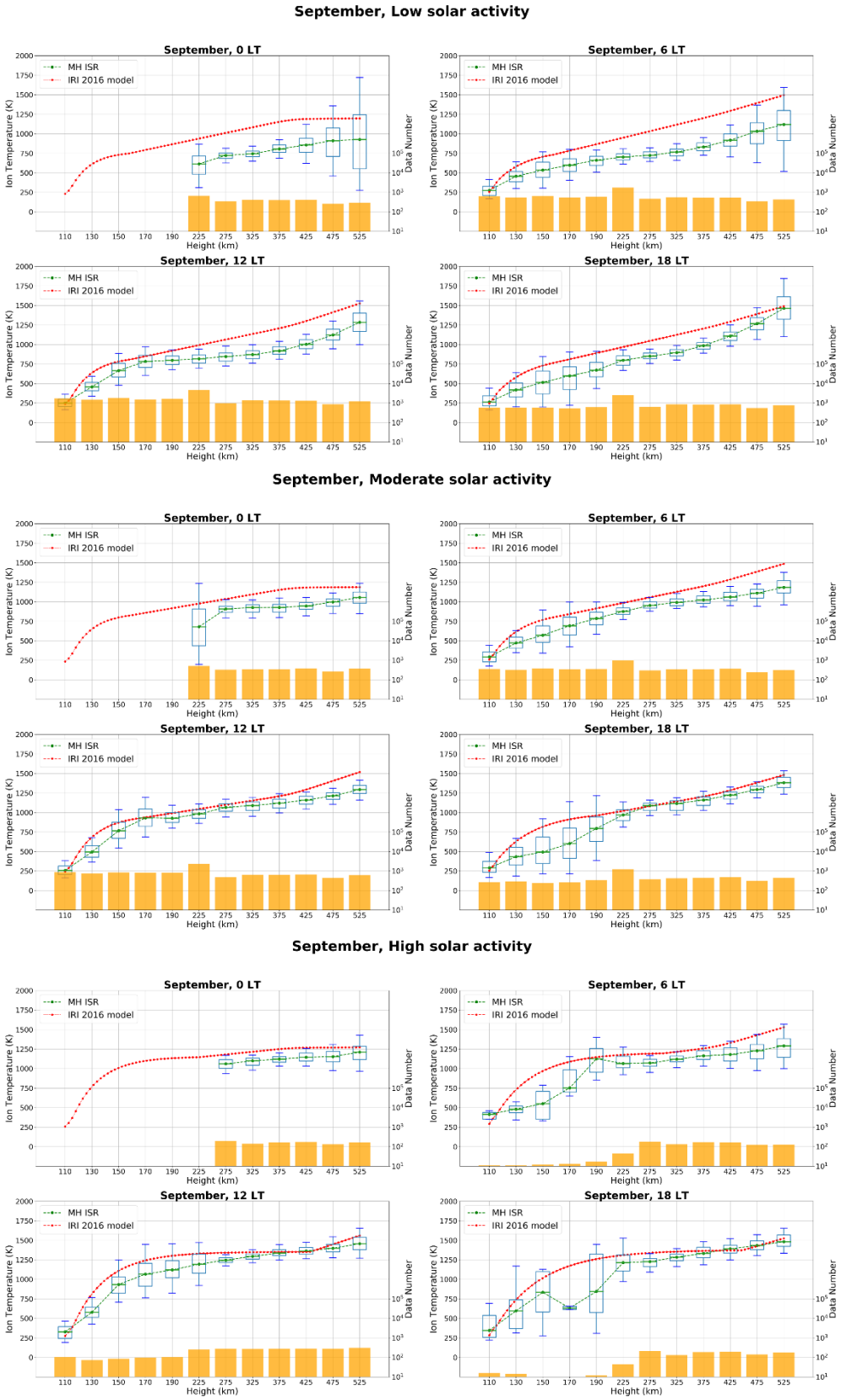

Figure 6: Same as Figure 4, but for September.

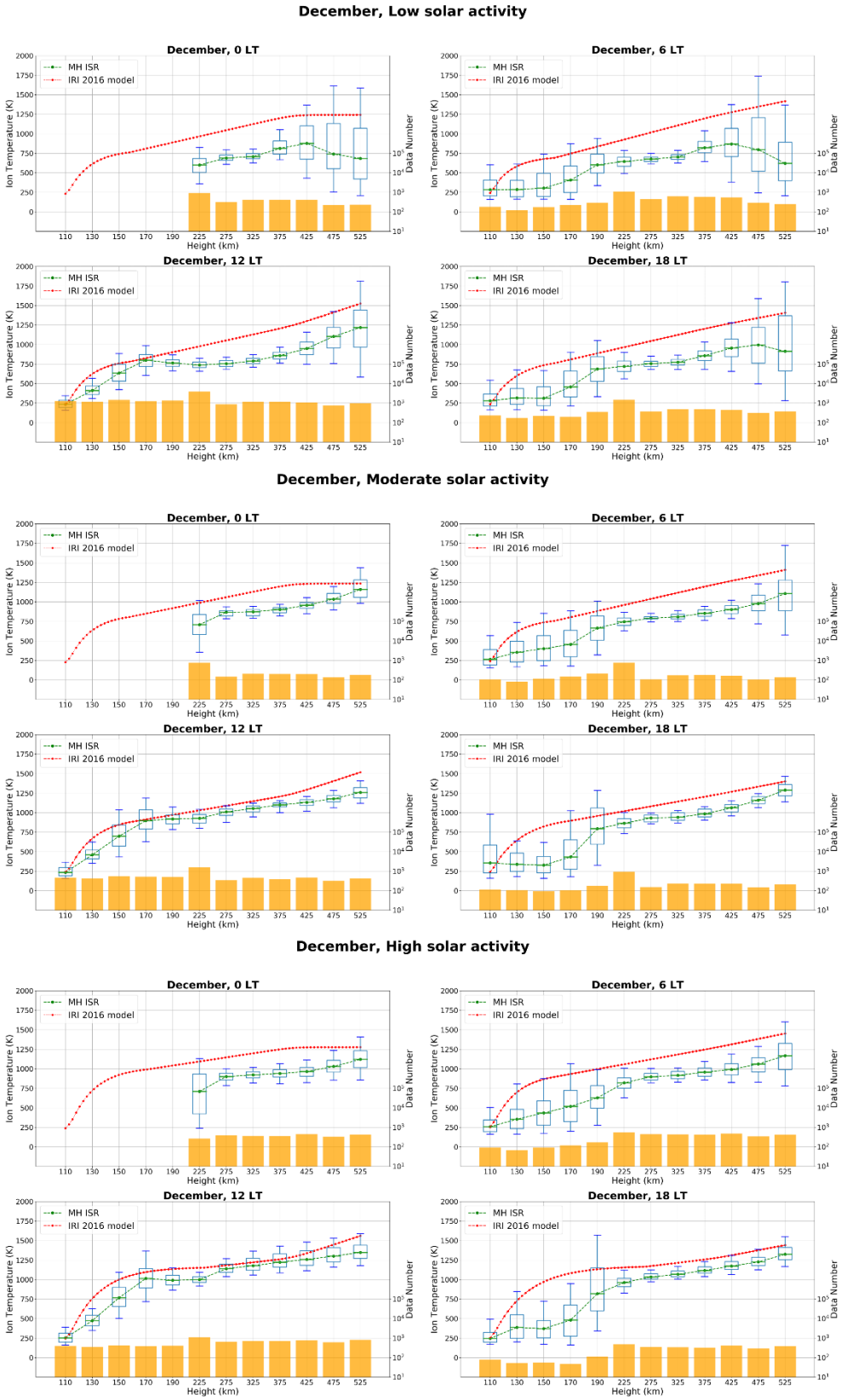

Figure 7: Same as Figure 4, but for December.

3.2 Statistical comparison between IRI and Millstone Hill ISR ion temperatures

To better highlight the differences between ion temperatures modeled by IRI and measured by Millstone Hill ISR, we here present a statistical analysis based on the results shown in Figures 4 to 7. Specifically, we calculate the residuals between median values of T_i by ISR and corresponding one modeled by IRI, for different altitude range, local time hour, season, and solar activity level. From residuals the following statistical parameters are calculated: Root Mean Square Error (RMSE) Eq. (6), Normalized Root Mean Square Error (NRMSE) Eq. (7), and Pearson correlation coefficient (R) Eq. (8).

$$\text{RMSE [K]} = \sqrt{\frac{\sum_{i=1}^{N}\left(T_{\text{iIRI},i} - T_{\text{iISR},i}\right)^2}{N}}, \tag{6}$$

$$\text{NRMSE [\%]} = \sqrt{\frac{\sum_{i=1}^{N}\left(\frac{T_{\text{iIRI},i} - T_{\text{iISR},i}}{T_{\text{iISR},i}} \cdot 100\right)^2}{N}}, \tag{7}$$

$$R = \frac{\text{cov}\left(T_{\text{iIRI}}, T_{\text{iISR}}\right)}{\sigma_{T_{\text{iIRI}}}\sigma_{T_{\text{iISR}}}} \in [-1,1], \tag{8}$$

In Eqs. (6)-(8), $T_{\text{i IRI}}$ represents the ion temperature modeled by IRI-2016, $T_{\text{i ISR}}$ the median ion temperature measured by ISR, N is the number of values on which the statistics are calculated, cov is the covariance matrix, and σ are the variances. Because of the large variations in the absolute values that the ion temperature exhibits, in Eq. (7) to give the same weight to differences between modeled and measured ion temperatures for both high and low absolute values, the normalization of the ion temperature differences is done in the summation.

Top panel of Figure 8 represents the statistical distribution of ion temperature residuals, with corresponding statistical values from residuals (mean and standard deviation) and from Eqs. (6)-(8), for the entire dataset of Figures 4 to 7. Bottom panel represents the scatterplot of measured vs modeled ion temperature values with corresponding measured error bars from first and third quartiles values. The red line in the bottom panel is the best linear fit line between measured and modeled values, with corresponding slope and intercept in the upper left box. Results of Figure 8 confirm the IRI overestimation of ion temperature values. In fact, the distribution of residuals is picked toward positive values (mean = 98 K) and the slope coefficient of the linear fit (0.866) is lower than one. Overall, IRI exhibits a substantial mismatch from measured values as highlighted by the RMSE (159.9 K) and NRMSE (22.36 %) values. However, most of such quite high differences are the result of the overall IRI overestimation; because, considering the correlation coefficient (0.927) and intercept (34.4 K) values, it is evident that IRI can catch the ion temperature variability for different geophysical conditions with a good degree of correlation.

The statistical analysis of Figure 8 was replicated by selecting different solar activity levels, season, local time hour, and altitude ranges. Corresponding statistical values are reported in Table 3. Results in Table 3 confirm the findings before highlighted by Figures 4 to 8. Notably:

1. Better IRI performances are for moderate and high solar activity levels compared to low;
2. Performances for the summer season (June) are by far better compared to other seasons. Equinoctial months (March and September) have very similar results, while by far worse are the IRI performances for the winter season (December);
3. As shown before, IRI describes very well the ion temperature at 12 LT. Performances for nighttime and solar terminator hours are instead quite similar and requiring improvements;
4. IRI performances for different altitude ranges are quite wavelike: NRMSE values increase from 100 to 160 km, then they decrease by reaching quite low values in the large range between 180 and 300 km, and then they increase again with height.

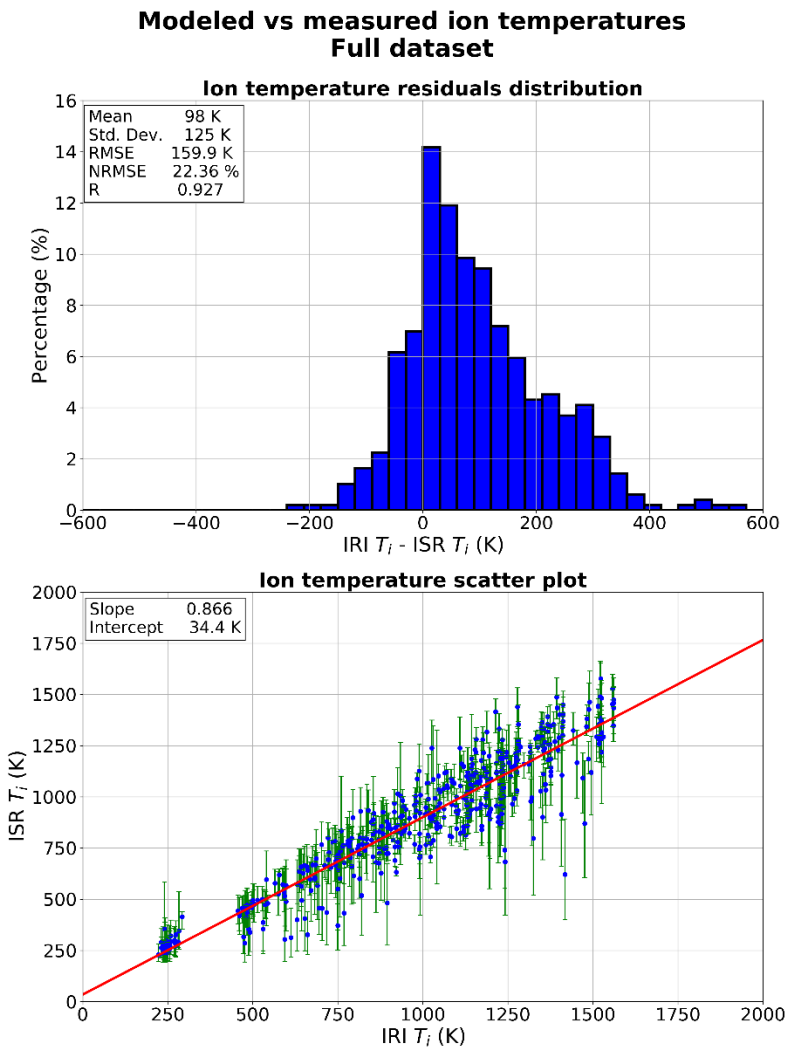

Figure 8: (top panel) Histogram of residuals between T_i values modeled by IRI and Millstone Hill ISR measured ones. *Y*-axis refers to the percentage of occurrences in bins. (bottom panel) Scatter plot of T_i values modeled by IRI and Millstone Hill ISR measured ones. The red line represents the best linear fit line. Millstone Hill ISR measured T_i values are those represented as boxplots in Figures 4 to 7, with corresponding median, first and third percentile calculated values.

Dataset	Residuals Mean [K]	Residuals Standard Deviation [K]	RMSE [K]	NRMSE [%]	R
Full dataset	98	125	159.9	22.36	0.927
Low Solar Activity	149	140	205.3	28.32	0.917
Moderate Solar Activity	76	100	126.0	17.72	0.952
High Solar Activity	64	115	131.8	19.05	0.934
March	81	131	154.3	17.14	0.918
June	59	66	88.7	9.15	0.982
September	78	110	135.4	15.84	0.947
December	169	146	224.2	36.16	0.896
100-120 km	-28	30	42.2	12.7	0.627
120-140 km	47	59	76.6	22.21	0.558
140-160 km	79	123	147.2	39.92	0.641
160-180 km	74	138	157.6	31.39	0.674
180-200 km	35	83	90.3	11.58	0.866
200-250 km	63	74	98.0	13.55	0.891
250-300 km	62	78	100.0	12.42	0.893
300-350 km	103	100	144.2	17.78	0.863
350-400 km	125	115	171.0	19.24	0.811
400-450 km	148	126	195.6	20.84	0.741
450-500 km	172	132	217.0	22.95	0.703
500-550 km	198	160	255.6	29.87	0.668
0 LT	175	99	201.5	24.48	0.776
6 LT	131	144	195.1	27.81	0.915
12 LT	52	101	114.1	11.35	0.962
18 LT	68	112	132.3	23.9	0.952

Table 3: Statistical results obtained by using T_i values modeled by IRI and measured by Millstone Hill ISR shown in Figures 4 to 7.

3.3 On the diurnal and seasonal variability of the ion temperature at 430 km of altitude

In Section 3.1 and 3.2, we highlighted some general features of the ion temperature as modeled by IRI in contrast to the ones measured by Millstone Hill ISR. In this section, we focus on the ion temperature at 430 km of altitude because, as described in Section 2.3, this is an anchor point for the modeled ion temperature vertical profile. Therefore, its modeling is of particular relevance for IRI. Modeled IRI ion temperature values at the 430 km anchor point (Eqs. (3)-(4)) are here compared to ISR observations measured in the range 400 – 450 km to highlight the diurnal and seasonal behavior for different solar activity levels.

Figure 9 represents the diurnal variability of the ion temperature at 430 km of height for different seasons and solar activity levels. By comparing the results for the same season but for different solar activity, it clearly emerges how IRI cannot describe the ion temperature variability as a function of the solar activity. The increase in T_i from low to high solar activity is clear from observations, while IRI shows only a slight solar activity dependence. Measured T_i observations exhibit a diurnal pattern more complex compared to the simple IRI nighttime to day-time trend (Eq. (5)). During equinoctial months the measured T_i values exhibit a well-defined diurnal maximum in the afternoon, during summer two maxima are observed in the morning and afternoon, while during winter a single maximum around noon is usually observed. All those diurnal patterns for different seasons are not described at all by IRI; thus, the need of implementing a seasonal dependence in the 430 km anchor point modeling and the need of improving the diurnal description to accommodate single or double maxima.

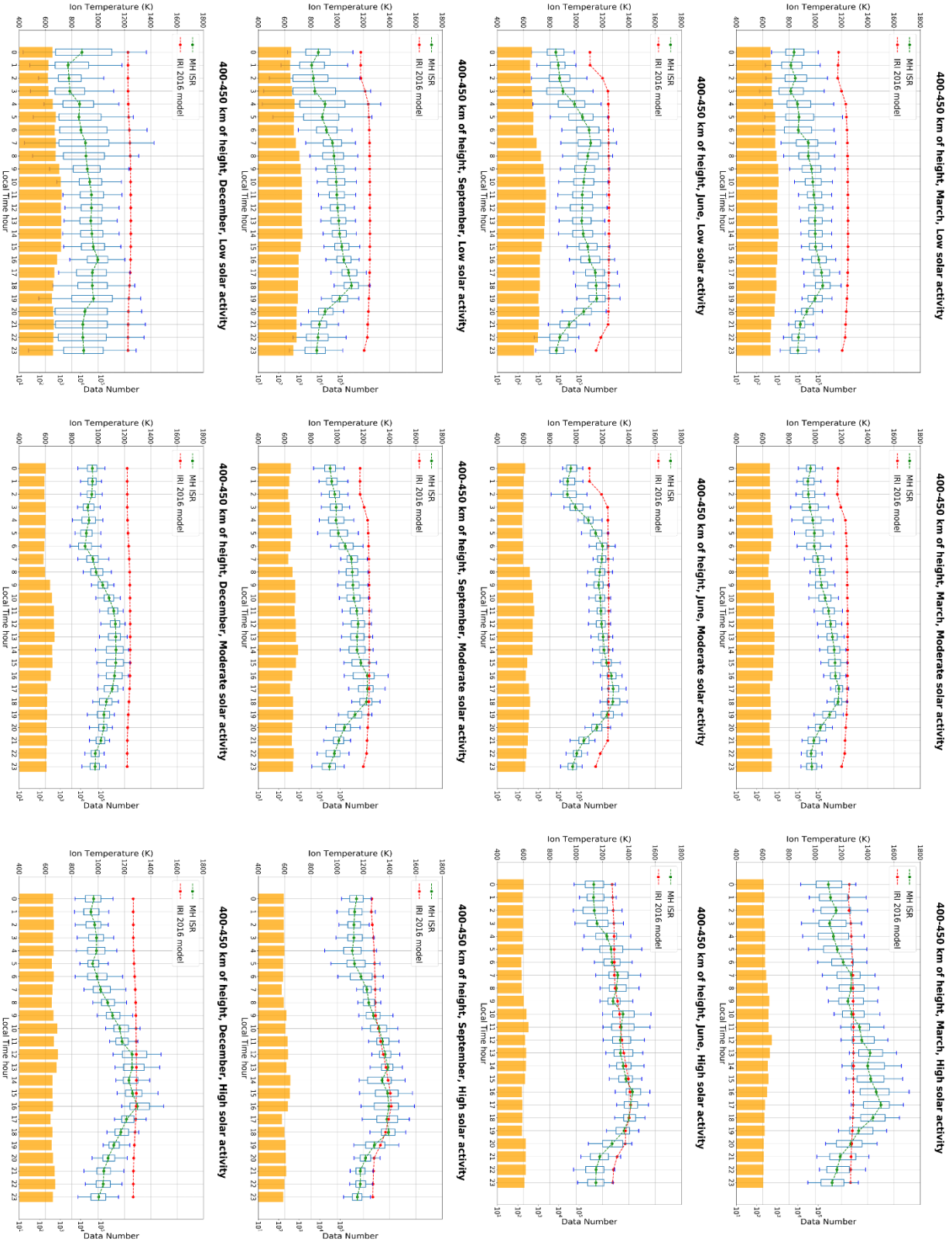

Figure 9: Boxplot analysis of ion temperatures recorded between 400 and 450 km of height as a function of LT hour, for the March (first row panels), June (second row panels), September (third row panels), and December (fourth row panels) month. First column for low solar activity, second column for moderate solar activity, and third column for high solar activity.

Figure 10 represents the seasonal dependence of the ion temperature anchor point at 430 km of altitude, for different local time hours and solar activity levels. Figure 10 highlights how measured T_i values exhibit a slight dependence on the season. This is particularly evident by looking at panels for nighttime (0 LT) and day-time (12 LT) hours. A more pronounced dependence on the season is visible for hours around solar terminator at dawn (6 LT) and dusk (18 LT). However, due to the fact that the solar terminator passage depends on the season, results for those sectors are affected by this. Anyway, IRI does not show any clear dependence on the season regardless the considered local time hour.

Generally, results for the 430 km anchor point confirm what emerged from the analysis of Sections 3.1 and 3.2, emphasizing the IRI difficulty in properly describing the diurnal, seasonal, and solar activity variability embedded in the ionospheric ion temperature observations.

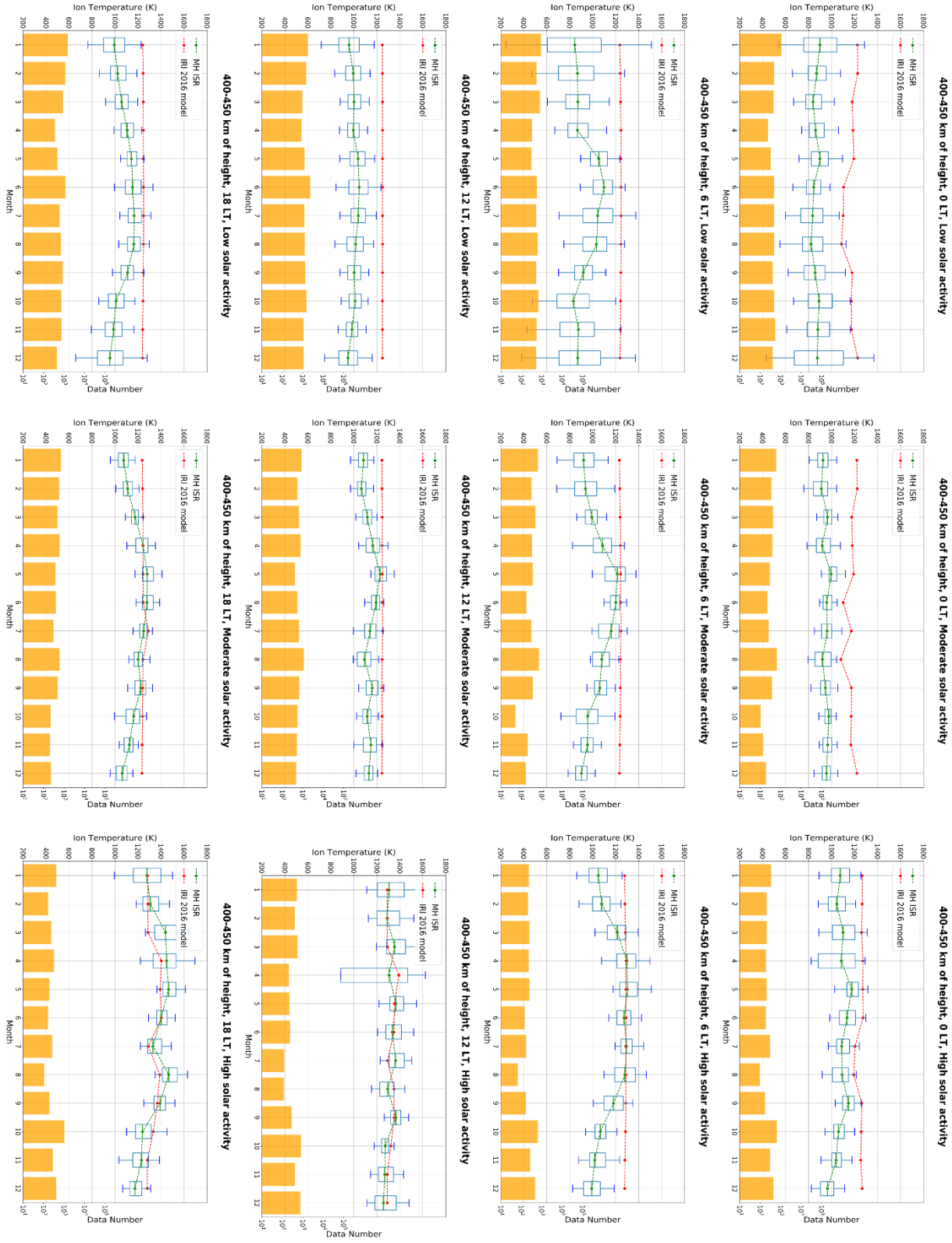

Figure 10: Boxplot analysis of ion temperatures recorded between 400 and 450 km of height as a function of the month of the year, for 0 LT (first row panels), 6 LT (second row panels), 12 LT (third row panels), and 18 LT (fourth row panels) hours. First column for low solar activity, second column for moderate solar activity, and third column for high solar activity.

4. Conclusions

In this paper, we analyzed ion temperature observations recorded by the Millstone Hill ISR for a very long period covering four solar cycles and compared them to IRI modeled values to shed light on the IRI performances and ability in describing the ion temperature dependence on altitude, local time, season, and solar activity level. The comparison is limited to magnetic quiet periods to describe the median climatological behavior.

The main results of our analysis are:

1. IRI overestimates the ion temperature for most of the cases. This is partly due to the fact that IRI does not explicitly account for the solar activity dependence in the ion temperature modeling. However, a large part of this overestimation can be due to the long-term cooling exhibited by the ionosphere in recent years. This is why, besides the need of including a solar activity dependence, the use of a modern ion temperature dataset is important;
2. IRI poorly describes the seasonal dependence and performances are highly variable for different seasons being better for summer and much worse for winter. The inclusion of a slight seasonal dependence in the IRI T_i model is desirable;
3. IRI includes only a simple day-to-night diurnal variation while observations show a more complex diurnal pattern that is also dependent on the season. Thus, the need of improving the diurnal description of the IRI ion temperature model;
4. The IRI anchor point at 430 km needs a more refined modeling of the diurnal, seasonal, and solar activity dependency.

Most of the above mentioned shortcomings might be mitigated by the use of a more recent dataset compared to that used by Bilitza (1981) in the development of the IRI ion temperature model. However, the seasonal and solar activity variability need to be implemented in IRI, and a more refined diurnal description is desirable. From this point of view, the dataset used in this work can be profitably used to this end.

It should be noted that the results shown in this work are valid for the Millstone Hill location (a geographic mid-latitude station, sub-auroral in magnetic coordinates); then, further studies are needed for different latitudes. However, this kind of studies are heavily constrained by the very sparse availability of ISR stations, thus the need of complementing them with satellite-based in-situ measurements to correctly describe the spatial variability of the ion temperature.

We have here highlighted climatological features of the ion temperature disregarding effects due to geomagnetic activity. Because disturbed magnetic conditions generally lead to the heating of the gas in the upper thermosphere and ionosphere, further studies are needed in order to introduce this variability in the IRI model.

Appendix

The IRI model applies the *Booker profile function* formalism (Booker, 1977) to describe the height and time variation of many ionospheric parameters (Bilitza, 1990).

In the Booker's approach, a mathematical variable $y(h)$ which steps from a value $y_1=y(h<h_s)$ to $y_2=y(h>h_s)$ at $h=h_s$, is represented by the *Epstep function*:

$$\begin{cases} y(h) = y_1 + \left(y_2 - y_1\right)\dfrac{1}{1+\exp(-x)} \\ x(h) = \dfrac{h-h_s}{d_s} \end{cases}, \qquad \text{(A1)}$$

where d_s determines the width of the transition region; thus producing a smooth transition between two different regimes, at the altitude h_s.

Specifically, the altitudinal profile of the variable y consists of more subsections in which y is constant; this is called *skeleton profile*, and can be represented by a sum of Epstep functions, stepping from subsection to subsection:

$$y(h) = y_0 + \sum_{j=1}^{m} \frac{\left(y_j - y_{j-1}\right)}{1 + \exp\left[-\frac{h - h_{s,j}}{d_{s,j}}\right]} , \tag{A2}$$

where m is the number of subsections, j is the index running on subsections, y_0=$y(h_0)$ where h_0 is the altitude starting point, $h_{s,j}$ are the altitudes at which steps occur, and $d_{s,j}$ the corresponding width parameters.

The integration of (A2) from h_0 to h gives $Y(h)$, i.e., the Booker profile function of y:

$$Y(h) = Y_0 + y_0\left(h - h_0\right) + \sum_{j=1}^{m} d_{s,j}\left(y_j - y_{j-1}\right)\ln\left[\frac{1 + \exp\left(\frac{h - h_{s,j}}{d_{s,j}}\right)}{1 + \exp\left(\frac{h_0 - h_{s,j}}{d_{s,j}}\right)}\right] . \tag{A3}$$

In (A3), Y_0 is the integration constant at h= h_0.

Acknowledgements

This work was conceived and developed during the school of the IRI 2019 Workshop (*Improving real-time ionospheric modelling in the European and African Sector*) held in Nicosia, Cyprus, on September 2019. It represents the *Problem F* assigned to the students of the *Group 6*, during the school. The authors are indebted to the organizers of the school of the IRI 2019 Workshop who fully supported their participation. Special acknowledgments are due to the local organizer Haris Haralambous and to his helper Christina Oikonomou, for the special care they showed towards students, and to Dieter Bilitza for his efforts in giving to students the possibility to attend the workshop.

A. Pignalberi is partially supported by the Italian MIUR-PRIN grant 2017APKP7T on Circumterrestrial Environment: Impact of Sun-Earth Interaction.

V. Truhlik was supported by grant LTAUSA17100 of the Ministry of Education, Youth and Sports of the Czech Republic

This publication uses data from Millstone Hill ISR made available via the public access portal of the Madrigal Database (http://millstonehill.haystack.mit.edu/). The authors are indebted to the observatory directors and operators for the significant investments of their time, effort, expertise, and funds needed to acquire and provide measurement data to academic research over the years. We thank Bill Rideout for preparing the data access script which was used to create data files for the present study. S. R. Zhang acknowledges US NSF Award AGS-1952737, US AFOSR MURI award FA9559-16-1-0364, and US ONR Grant N00014-17-1-2186 to support for his effort.

The IRI team is acknowledged for developing and maintaining the IRI model and for giving access to the corresponding Fortran code via the IRI website (http://irimodel.org/).

Solar and magnetic activity indices used in this study were downloaded from OMNIWeb Data Explorer website (https://omniweb.gsfc.nasa.gov/form/dx1.html) maintained by the Space Physics Data Facility of the Goddard Space Flight Center (NASA).

References

Banks, P. M. (1967) Ion temperature in the upper atmosphere, *J. Geophys. Res.*, 72(13), 3365–3385, doi:10.1029/JZ072i013p03365.

Bilitza, D. (1981) Models for ionospheric electron and ion temperature, in K. Rawer, J. V. Lincoln, and R. O. Conkright, International Reference Ionosphere-IRI 79, World Data Center A for Solar-Terrestrial Physics, *Report UAG-82*, 245 pp., Boulder, Colorado, USA, (downloadable from http://www.irimodel.org/).

Bilitza, D. (1984) The Atmosphere Explorer C ionospheric temperatures: Dependences and representation, in *Report UAG-90*, World Data Center A for Solar-Terrestrial Physics, Boulder, Colorado, USA, (downloadable from http://www.irimodel.org/).

Bilitza, D. (1987) Description of the mean behavior of ionospheric plasma temperature, *Adv. Space Res.*,7(6), 93-98, https://doi.org/10.1016/0273-1177(87)90280-8.

Bilitza, D. (1990) International Reference Ionosphere, *National Space Science Data Center, Report 90-22*, Greenbelt, Maryland, USA, (downloadable from http://www.irimodel.org/).

Bilitza, D., and W. R. Hoegy (1990), Solar activity variations of ionospheric plasma temperatures, *Adv. Space Res.*, 10(8), 81– 90, https://doi.org/10.1016/0273-1177(90)90190-B.

Bilitza, D. (1991) Electron and ion temperature data for ionosphere modelling, *Adv. Space Res.*, 11(10), 139-148, https://doi.org/10.1016/0273-1177(91)90336-I.

Bilitza, D., Rawer, K., Bossy, L., and Gulyaeva, T. (1993) International Reference Ionosphere - Past, Present, Future: II. Plasma Temperatures, Ion Composition, and Ion Drift, *Adv. Space Res.*, 13(3), 15-23, https://doi.org/10.1016/0273-1177(93)90241-3.

Bilitza, D., Truhlik, V., Richards, P., Abe, T., and Triskova, L. (2007) Solar cycle variation of mid-latitude electron density and temperature: Satellite measurements and model calculations, *Adv. Space Res.*, 39(5), 779–789, doi:10.1016/j.asr.2006.11.022.

Bilitza, D., Altadill, D., Truhlik, V., Shubin, V., Galkin, I., Reinisch, B., and Huang, X. (2017) International Reference Ionosphere 2016: From ionospheric climate to real-time weather predictions, *Space Weather*, 15, 418-429, doi:10.1002/2016SW001593.

Bilitza, D. (2018) IRI the International Standard for the Ionosphere, *Adv. Radio Sci.*, 16, 1–11, https://doi.org/10.5194/ars-16-1-2018.

Booker, H.G. (1977) Fitting of multi-region ionospheric profiles of electron density by a single analytic function of height, *J. Atmos. Terr. Phys.*, 39(5), 619–623, https://doi.org/10.1016/0021-9169(77)90072-1.

Buonsanto, M.J. (1989) Comparison of incoherent scatter observations of electron density, and electron and ion temperature at Millstone Hill with the International Reference Ionosphere, *J. Atmos. Terr. Phys.*, 51(5), 441–468, https://doi.org/10.1016/0021-9169(89)90125-6.

Evans, J.V. (1967) Midlatitude electron and ion temperatures at sunspot minimum, *Planet. Space Sci.*, 15(10), 1157-1570, https://doi.org/10.1016/0032-0633(67)90089-X.

Evans, J. V. (1969) Theory and practice of ionosphere study by Thomson scatter radar, *Proceedings of the IEEE*, 57 (4), 496-530, doi: 10.1109/PROC.1969.7005.

Evans, J.V. (1970) Millstone Hill Thomson scatter results for 1965, *Planet. Space Sci.*, 18(8), 1225-1253, https://doi.org/10.1016/0032-0633(70)90214-X.

Holt, J. M., S.-R. Zhang, and M. J. Buonsanto (2002) Regional and local ionospheric models based on Millstone Hill incoherent scatter radar data, *Geophys. Res. Lett.*, 29(8), 1207, doi:10.1029/2002GL014678.

Holt, J. M., and S. R. Zhang (2008) Long-term temperature trends in the ionosphere above Millstone Hill, *Geophys. Res. Lett.*, 35, L05813, doi:10.1029/2007GL031148.

Laštoviča, J. (2017) A review of recent progress in trends in the upper atmosphere, *J. Atmos. Solar-Terr. Phys.*, 163, 2- 13, https://doi.org/10.1016/j.jastp.2017.03.009.

Oliver, W. L., Takami, T., Fukao, S., Sato, T., Yamamoto, M., Tsuda, T., Nakamura, T., and Kato, S. (1991) Measurements of ionospheric and thermospheric temperatures and densities with the middle and upper atmosphere radar, *J. Geophys. Res.*, 96(A10), 17827– 17838, doi:10.1029/91JA01654.

Otsuka, Y., Kawamura, S., Balan, N., Fukao, S., Bailey, G.J. (1998) Plasma temperature variations in the ionosphere over the middle and upper atmosphere radar, *J. Geophys. Res.*, 103(A9), 20705-20713, doi:10.1029/98JA01748.

Picone, J.M., Hedin, A.E., Drob, D.P., & Aikin, A.C. (2002) NRLMSISE-00 empirical model of the atmosphere: Statistical comparisons and scientific issues, *J. Geophys. Res.*, 107(A12), 1468, doi:10.1029/2002JA009430.

Ratcliffe, J.A. (1972) An introduction to the ionosphere and magnetosphere. *Cambridge University Press*, Cambridge, Great Britain.

Rishbeth, H., and Garriott, O. (1969) Introduction to ionospheric physics. *Academic Press*, International geophysics series v. 14, New York, USA.

Roble, R.G. (1975) The calculated and observed diurnal variation of the ionosphere over Millstone Hill on March 23–24, 1970, *Planet. Space Sci.*, 23(7), 1017-1033, https://doi.org/10.1016/0032-0633(75)90192-0.

Roble, R. G., Stewart, A. I., Torr, M. R., Rusch, D. W., and Wand, R. H. (1978) The calculated and observed ionospheric properties during Atmospheric Explorer-C satellite crossings over Millstone Hill. *J. Atmos. Terr. Phys.*, 40(1), 21-33, doi:10.1016/0021-9169(78)90105-8.

Rostoker, G. (1972) Geomagnetic Indices, *Rev. Geophys. Space Phys.*, 10(4), 935-950, doi:10.1029/RG010i004p00935.

Schunk, R. W., and A. F. Nagy (1978) Electron temperatures in the F region ionosphere: Theory and observations, *Rev. Geophys.*, 16(3), 355– 399, doi:10.1029/RG016i003p00355.

Tapping, K. F. (2013) The 10.7 cm solar radio flux ($F_{10.7}$), *Space Weather*, 11, 394-406, doi:10.1002/swe.20064.

Truhlik, V., Bilitza, D., and Triskova, L. (2009) Latitudinal variation of the topside electron temperature at different levels of solar activity, *Adv. Space Res.*, 44(6), 693–700, doi:10.1016/j.asr.2009.04.029.

Truhlik, V., Bilitza, D., and Triskova, L. (2012) A new global empirical model of the electron temperature with inclusion of the solar activity variations for IRI, *Earth Planets Space*, 64, 531–543, https://doi.org/10.5047/eps.2011.10.016.

Truhlik, V., Bilitza, D., and Třisková, L. (2015) Towards better description of solar activity variations in IRI ion composition model, *Adv. Space Res.*,55(8), 2099–2105, doi:10.1016/j.asr.2014.07.033.

Willmore, A.P. (1970) Electron and ion temperatures in the ionosphere. *Space Sci. Rev.*, 11**,** 607–670, https://doi.org/10.1007/BF00177027.

Zhang, S.-R., and J. M. Holt (2004) Ionospheric plasma temperatures during 1976– 2001 over Millstone Hill, *Adv. Space Res.*, 33(6), 963– 969, doi:10.1016/j.asr.2003.07.012.

Zhang, S.-R. and J. M. Holt (2007), Ionospheric Climatology and Variability from Long-term and Multiple Incoherent Scatter Radar Observations: Climatology in Eastern American Sector, *J. Geophys. Res.*, 112, A06328, doi:10.1029/2006JA012206.

Zhang, S.-R. and J. M. Holt (2008) Ionospheric climatology and variability from long-term and multiple incoherent scatter radar observations: variability, *Annales Geophysicae*, 26, 1525-1537, doi:10.5194/angeo-26-1525-2008.

Zhang, S.-R. and J. M. Holt (2013) Long-term ionospheric cooling: dependency on local time, season, solar activity and geomagnetic activity, *J. Geophys. Res. Space Physics*, 118, 3719-3730, doi:10.1002/jgra.50306.

Zhang, S.-R., J. M. Holt, A. M. Zalucha, and C. Amory-Mazaudier (2004) Midlatitude ionospheric plasma temperature climatology and empirical model based on Saint Santin incoherent scatter radar data from 1966 to 1987, *J. Geophys. Res.*, 109, A11311, doi:10.1029/2004JA010709.

Zhang, S.-R., J. M. Holt, A. P. van Eyken, M. McCready, C. Amory-Mazaudier, S. Fukao, and M. Sulzer (2005a) Ionospheric local model and climatology from long-term databases of multiple incoherent scatter radars, *Geophys. Res. Lett.*, 32, L20102, doi:10.1029/2005GL023603.

Zhang, S.-R., J. M. Holt, P. J. Erickson, F. D. Lind, J. C. Foster, A. P. van Eyken, Y. Zhang, L. J. Paxton, W. C. Rideout, L. P. Goncharenko, and G. R. Campbell (2005b) October 2002 30-day Incoherent Scatter Radar Experiments at Millstone Hill and Svalbard and Simultaneous GUVI/TIMED Observations, *Geophys. Res. Lett.*, 32, L01108, doi:10.1029/2004GL020732.

Zhang, S.-R., J. M. Holt, D. Bilitza, A. P. van Eyken, M. McCready, C. Amory-Mazaudier, S. Fukao, and M. Sulzer (2007) Multiple-site comparisons between models of incoherent scatter radar and IRI, *Adv. Space Res.*, 39(5), 910-917, doi:10.1016/j.asr.2006.05.027.

Zhang, S.-R., J. M. Holt, and J. Kurdzo (2011) Millstone Hill ISR observations of upper atmospheric long-term changes: height dependency, *J. Geophys. Res.*, 116, A00H05, doi:10.1029/2010JA016414.

Zhang, S.-R., Holt, J. M., Erickson, P. J., Goncharenko, L. P., Nicolls, M. J., McCready, M., & Kelly, J. (2016) Ionospheric ion temperature climate and upper atmospheric long-term cooling, *J. Geophys. Res.*, 121, 8951–8968. http://doi.org/10.1002/2016JA022971.

Zhang, S.-R., Holt, J. M., Erickson, P. J., & Goncharenko, L. P. (2018) Comments on "Long-term variations of exospheric temperature inferred from foF1 observations: A comparison to ISR T_i trend estimates" by Perrone and Mikhailov. *J. Geophys. Res.*, 123, 4467– 4473. https://doi.org/10.1029/2017JA024948.